

Genomic and Functional Fidelity of Small Cell Lung Cancer Patient-Derived Xenografts



Benjamin J. Drapkin¹, Julie George², Camilla L. Christensen³, Mari Mino-Kenudson⁴, Ruben Dries³, Tilak Sundaresan^{1,5}, Sarah Phat¹, David T. Myers¹, Jun Zhong¹, Peter Igo¹, Mehlika H. Hazar-Rethinam¹, Joseph A. Licausi^{1,5}, Maria Gomez-Caraballo¹, Marina Kem^{1,4}, Kandarp N. Jani³, Roxana Azimi¹, Nima Abedpour^{2,6}, Roopika Menon⁷, Sotirios Lakis⁷, Rebecca S. Heist^{1,5,8}, Reinhard Büttner⁹, Stefan Haas¹⁰, Lecia V. Sequist^{1,5,8}, Alice T. Shaw^{1,5,8}, Kwok-Kin Wong¹¹, Aaron N. Hata^{1,5,8}, Mehmet Toner^{5,12,13,14}, Shyamala Maheswaran^{1,5,13}, Daniel A. Haber^{1,5,8,15}, Martin Peifer^{2,6}, Nicholas Dyson^{1,5}, Roman K. Thomas^{2,9,16}, and Anna F. Farago^{1,5,8}

ABSTRACT

Small cell lung cancer (SCLC) patient-derived xenografts (PDX) can be generated from biopsies or circulating tumor cells (CTC), though scarcity of tissue and low efficiency of tumor growth have previously limited these approaches. Applying an established clinical-translational pipeline for tissue collection and an automated microfluidic platform for CTC enrichment, we generated 17 biopsy-derived PDXs and 17 CTC-derived PDXs in a 2-year timeframe, at 89% and 38% efficiency, respectively. Whole-exome sequencing showed that somatic alterations are stably maintained between patient tumors and PDXs. Early-passage PDXs maintain the genomic and transcriptional profiles of the founder PDX. *In vivo* treatment with etoposide and platinum (EP) in 30 PDX models demonstrated greater sensitivity in PDXs from EP-naïve patients, and resistance to EP corresponded to increased expression of a *MYC* gene signature. Finally, serial CTC-derived PDXs generated from an individual patient at multiple time points accurately recapitulated the evolving drug sensitivities of that patient's disease. Collectively, this work highlights the translational potential of this strategy.

SIGNIFICANCE: Effective translational research utilizing SCLC PDX models requires both efficient generation of models from patients and fidelity of those models in representing patient tumor characteristics. We present approaches for efficient generation of PDXs from both biopsies and CTCs, and demonstrate that these models capture the mutational landscape and functional features of the donor tumors. *Cancer Discov*; 8(5); 600–15. ©2018 AACR.

INTRODUCTION

Small cell lung cancer (SCLC) is a high-grade neuroendocrine malignancy with a 5-year overall survival of approximately 5%. Among patients diagnosed with metastatic (extensive stage) disease, the median overall survival is

approximately 9 to 11 months with standard treatment (1–4). Because neither surgical resection nor repeat tumor biopsies are standard of care in metastatic SCLC, access to clinically relevant tissue is limited. Instead, SCLC research has relied heavily on preclinical models such as established cell lines, genetically engineered mouse models (GEMM), and more recently, patient-derived xenografts (PDX; refs. 5–8).

PDX models, generated via direct implantation of patient tumor tissue into a recipient mouse, have several theoretical advantages over other preclinical models. First, bypass of an *in vitro* intermediate potentially avoids bottleneck events or selection for fitness in the *in vitro* environment (9). Second, molecular and functional phenotypes can be correlated directly with patient characteristics and clinical response to therapies. The increasing use of PDX models in SCLC research underscores their importance to the field (5, 10, 11).

Many solid tumors shed malignant cells into circulation, and collection of these rare circulating tumor cells (CTC) enables noninvasive serial tumor sampling (12–15). CTCs are highly abundant in patients with SCLC compared with patients with other solid tumor malignancies (16–18), and CTC number is prognostic and reflects the changing burden of disease over the course of treatments (19). The development of PDX models from CTCs isolated by Ficoll density gradient marked a significant advance for generation of SCLC preclinical models (20), eliminating the need for surgical resection or invasive biopsy. To date, a handful of CTC-derived SCLC PDX models have been described (11, 20). These were generated from samples that had a minimum of 400 CTCs per 7.5 mL blood, but the widespread application of this methodology to generate SCLC models is yet to be reported. Although live CTC enrichment can be achieved through application of microfluidic devices (21), this approach has not yet been used for PDX generation.

Although the application of SCLC PDXs for preclinical studies is increasingly common, further characterization is needed

¹Massachusetts General Hospital Cancer Center, Boston, Massachusetts.

²Department of Translational Genomics, Center of Integrated Oncology Cologne-Bonn, Medical Faculty, University of Cologne, Cologne, Germany.

³Dana-Farber Cancer Institute, Boston, Massachusetts. ⁴Department of

Pathology, Massachusetts General Hospital, Boston, Massachusetts. ⁵Harvard

Medical School, Boston, Massachusetts. ⁶Center for Molecular Medicine

Cologne (CMCC), University of Cologne, Cologne, Germany. ⁷NEO New

Oncology GmbH, Cologne, Germany. ⁸Department of Medicine, Massachusetts

General Hospital, Boston, Massachusetts. ⁹Department of Pathology, University

Hospital Cologne, Cologne, Germany. ¹⁰Computational Molecular

Biology Group, Max Planck Institute for Molecular Genetics, Berlin, Germany.

¹¹Department of Hematology and Oncology, New York University

Langone Medical School, New York, New York. ¹²Center for Engineering

in Medicine, Massachusetts General Hospital, Boston, Massachusetts.

¹³Department of Surgery, Massachusetts General Hospital, Boston, Massachusetts.

¹⁴Shriners Hospital for Children, Boston, Massachusetts. ¹⁵Howard

Hughes Medical Institute, Chevy Chase, Maryland. ¹⁶German Cancer

Research Center, German Cancer Consortium (DKTK), Heidelberg, Germany.

Note: Supplementary data for this article are available at Cancer Discovery Online (<http://cancerdiscovery.aacrjournals.org/>).

B.J. Drapkin and J. George are co-first authors of this article.

Current address for T. Sundaresan: Kaiser Permanente, San Francisco, CA; current address for P. Igo: Sentien Biotechnologies, Lexington, MA; and current

address for M. Gomez-Caraballo: Duke University Medical School, Durham, NC.

Corresponding Authors: Anna F. Farago, Massachusetts General Hospital

Cancer Center, 55 Fruit Street, Yawkey 7B, Boston, MA 02114. Phone: 617-

643-3472; Fax: 617-726-0453; E-mail: afarago@partners.org; and Roman

K. Thomas, Universität zu Köln, Abteilung Translationale Genomik, Weyertal

115 b, 50931 Köln, Germany. Phone: 49-221-478-98777; Fax: 49-221-

478-97902; E-mail: roman.thomas@uni-koeln.de

doi: 10.1158/2159-8290.CD-17-0935

©2018 American Association for Cancer Research.

to assess how accurately these models reproduce properties of the human disease. SCLC tumors are known to have extensive genomic alterations and a high mutational burden (22–24). Furthermore, biallelic inactivation of *TP53* and *RB1* is nearly universal in SCLCs (22). These changes may undermine genomic stability, raising the concern that SCLC genomes may acquire additional genomic alterations and evolve rapidly when passaged in mice. The recent finding that PDX models of diverse tumor types acquire mutations with serial passages underscores this concern (25). Although copy-number variations appear conserved between CTCs and CTC-derived PDXs in a limited number of cases examined (20), whether the genomes of CTC-derived PDX models of SCLC accurately mirror the patient's biopsy has not yet been rigorously investigated.

Functional characterization of SCLC PDXs is also a critical metric of the utility of these models. SCLC tumors are classically highly sensitive to etoposide and platinum (EP; ref. 1). Among three PDX models treated with EP (20), responses in the models correlated with those in the donor patients. However, more extensive testing of how well SCLC PDXs recapitulate chemotherapy sensitivity and acquired resistance, and how these profiles correlate with underlying molecular signatures, is needed.

Here, we describe the efficient generation of 34 PDX models of SCLC in a 2-year timeframe, utilizing both tissue biopsies and blood samples processed with an automated microfluidic device. We show that these models can be generated at high efficiency from CTCs, irrespective of enumeration, and that they faithfully recapitulate both the genomic and functional features of patient tumors at the time of model generation. We quantified *in vivo* sensitivity to EP in 30 PDX models and found that models derived from EP-naïve patients were more sensitive than models from patients previously treated with EP. Further transcriptome profiling of models revealed that increasing EP resistance correlates closely with activation of a *MYC* transcription program. Finally, serial models derived from an individual patient at multiple time points reflect the evolving clinical response of that patient's tumor, emphasizing the potential application of these approaches toward studying acquired resistance.

RESULTS

Construction of an SCLC PDX Panel

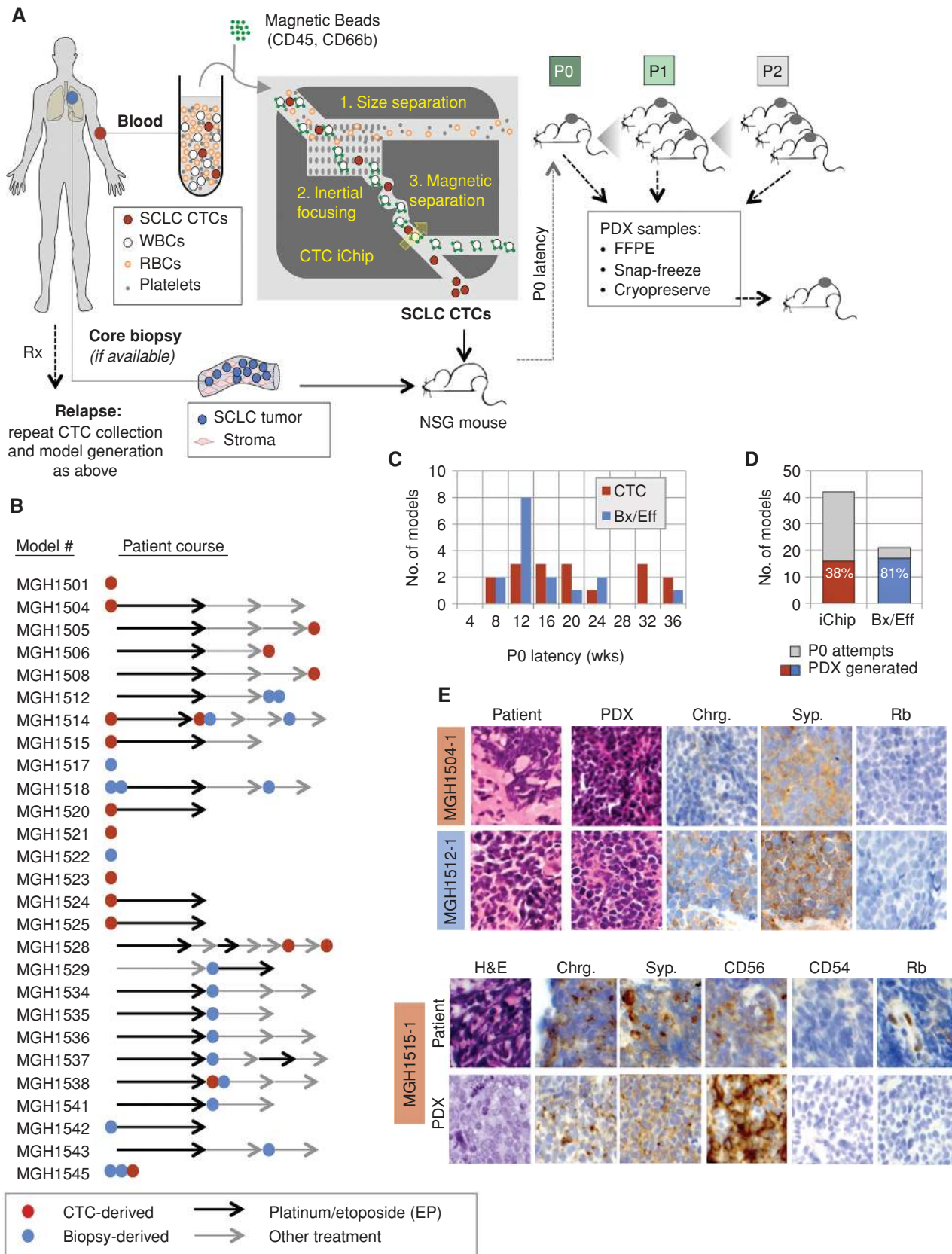
Biopsy- and CTC-derived PDX models from patients with SCLC have been described (5, 20, 26), but there remains a paucity of SCLC models from patients with detailed correlative

clinical data. PDXs generated after patient relapse are especially scarce because these patients rarely undergo a clinically indicated biopsy. Currently, there are no published sets of sequential PDX models from patients with SCLC that can be used to study disease evolution. The key parameter, as yet uncertain, is the success rate of PDX generation from routine blood samples and tissue biopsies. We therefore focused on a population of patients with SCLC selected only on the basis of having clinically progressive disease at the time of tissue or blood collection.

Between June 2014 and June 2016, we enrolled patients with known or suspected SCLC on Institutional Review Board (IRB)-approved protocols for collection of clinical data, blood, and tissue. Blood samples for PDX development were taken at the time of initial diagnosis or progression after a prior therapy, but not while a patient's disease was currently responding to treatment. For each patient, SCLC CTCs were isolated from a 15 to 20 mL whole blood sample with the CTC-iChip^{neg} device (27), with a typical transport time from patient to laboratory of 60 to 90 minutes. The CTC-iChip^{neg} first excludes plasma, unbound antibody-coated beads, platelets, and red blood cells through microfluidic size-based separation, and then directs nucleated cells (leukocytes and CTCs) into a single-cell stream through inertial focusing microfluidic channels, thereby enabling the highly efficient magnetic separation of anti-CD45/CD66b-tagged leukocytes (27, 28). The resulting product is highly enriched (10^4 – 10^5 -fold) for unmanipulated and potentially viable CTCs (Fig. 1A). CTC-enriched products were immediately prepared for subcutaneous injection into NOD/SCID gamma (NSG) mice. Animals were then monitored for tumor growth over a period of at least 6 months. From 42 processed blood samples, 16 animals developed palpable tumors, for an overall tumor growth efficiency of 38% [95% confidence interval (CI), 24–54] and a median latency of 115 days (Fig. 1B–D). Following previously described protocols as done in ref. 20, we generated one model from CTCs isolated by Ficoll gradient (Supplementary Table S1).

In a parallel effort, we also sought to generate PDX models of SCLC from patients undergoing a tissue biopsy. One extra core tumor biopsy was collected from patients with known or suspected SCLC when they were undergoing a biopsy for clinical purposes. Core tumor specimens, generally 19 to 22 gauge and approximately 4 to 8 mm in length, were obtained from patients and implanted into the flanks of NSG mice within 2 hours of the biopsy procedure (Fig. 1A; Supplementary Table S2). From 18 implanted specimens from patients with confirmed SCLC, 16 developed into xenograft

Figure 1. Generation of a population of SCLC PDX models. **A**, Strategy for SCLC PDX development. PDX models were initiated from whole blood via CTC isolation (red, top), core tumor biopsies (blue, bottom), or effusion specimens. Whole blood samples were processed via the CTC-iChip^{neg} device, which enriches CTCs in a three-step process: (1) separation of nonnucleated cells and plasma by size hydrodynamic diameter using a microarray of posts, (2) inertial focusing through an asymmetric serpentine channel to position cells in a single line, and (3) negative selection of leukocytes decorated with anti-CD45/CD66b magnetic beads by magnetic separation (yellow arrow = magnetic deflection). Biopsy, effusion, and CTC samples were injected s.c. into the flanks of NSG mice, monitored for tumor emergence (PO latency), and then serially passaged (P1, P2). Tumor samples were obtained for molecular and pathologic analysis and for cryopreservation of the model. **B**, Panel of SCLC PDX models with abstracted patient clinical courses. Models derived from either CTCs (red circles) or biopsies/effusions (blue circles) were generated at various time points throughout the treatment of the patient (arrows). Arrows are not drawn to scale with respect to time on treatments. **C**, Latency to (PO) tumor emergence for models initiated from June 2014 to June 2016. **D**, Efficiency of PDX generation from CTCs and biopsies (Bx)/effusions (Eff). Total attempts in gray, successful in color. **E**, Pathologic confirmation of SCLC. Shown are SCLC histology (hematoxylin and eosin staining) comparison between biopsy and PDX derived from either CTCs (MGH1504-1) or biopsy (MGH1512-1), as well as IHC stains for neuroendocrine markers and of nuclear RB1. Direct comparison of histology and IHC stains in a patient sample and corresponding CTC-derived PDX model (MGH1515-1) are also shown. Additional examples are shown in Supplementary Fig. S1. Chrg., chromogranin; FFPE, formalin-fixed, paraffin embedded; RBC, red blood cell; Synp., synaptophysin; WBC, white blood cell.



Downloaded from <http://aacrjournals.org/cancerdiscovery/article-pdf/8/5/600/1839874/600.pdf> by guest on 27 August 2022

Table 1. Characteristics of PDX models selected for whole-exome sequencing

Model	PDX type ^a	Biopsy to model initiation (days) ^b	P0 latency (days) ^c	Patient clinical stage	Patient prior therapies
MGH1504-1	CTC	3	160	LS	None
MGH1512-1	Biopsy	0	60	ES	EC, irinotecan
MGH1514-1	CTC	4	130	ES	None
MGH1515-1	CTC	8	138	ES	None
MGH1518-1	Biopsy	0	81	ES	None
MGH1525-1	CTC	1	45	ES	None
MGH1528-1	CTC	-	107	ES	EC, topotecan, EC, paclitaxel, exp1, exp2, vinorelbine

Abbreviations: EC, carboplatin and etoposide; ES, extensive stage; exp, experimental therapy on clinical trial; LS, limited stage.

^aPDX type indicates if the model is CTC-derived or biopsy-derived.

^bFor all CTC-derived models except MGH1528-1, a biopsy was collected near the time of CTC collection, without any intervening therapy, and these were the patient tumor samples used for whole-exome sequencing. Time from biopsy to model initiation is shown.

^cP0 latency indicates time from tissue implantation to when a tumor was first palpated on the flank of the recipient mouse.

tumors within 6 months, for an overall growth efficiency of 89% (95% CI, 74–99) and a median latency of 78 days (Fig. 1B and C; Supplementary Table S1). In addition, one PDX model was generated from a malignant pleural effusion.

Once the founder (P0) PDX tumors reached a size of approximately 1 to 1.5 cm in diameter, they were dissected, portions of the tumor material were passaged into additional NSG mice, and tissue was preserved for further analyses (Fig. 1A). The latency for growth of passaged tumors was typically 2 to 6 weeks, considerably shorter than for P0 tumor growth. There were no model failures after initial P0 tumor emergence; all xenografts were successfully maintained for at least two passages, and all attempts at regrowth from cryopreserved specimens were successful (Supplementary Table S1). In total, within the specified timeframe for tissue collection, 34 SCLC models were established from 27 separate patients (Fig. 1B). These models were generated from patients with a range of time points in their clinical course of SCLC, including 15 models from patients prior to receiving any SCLC-directed therapy, and 19 from patients after at least one line of therapy. From 3 patients, serial models were developed at multiple points over the course of their treatments (Fig. 1B).

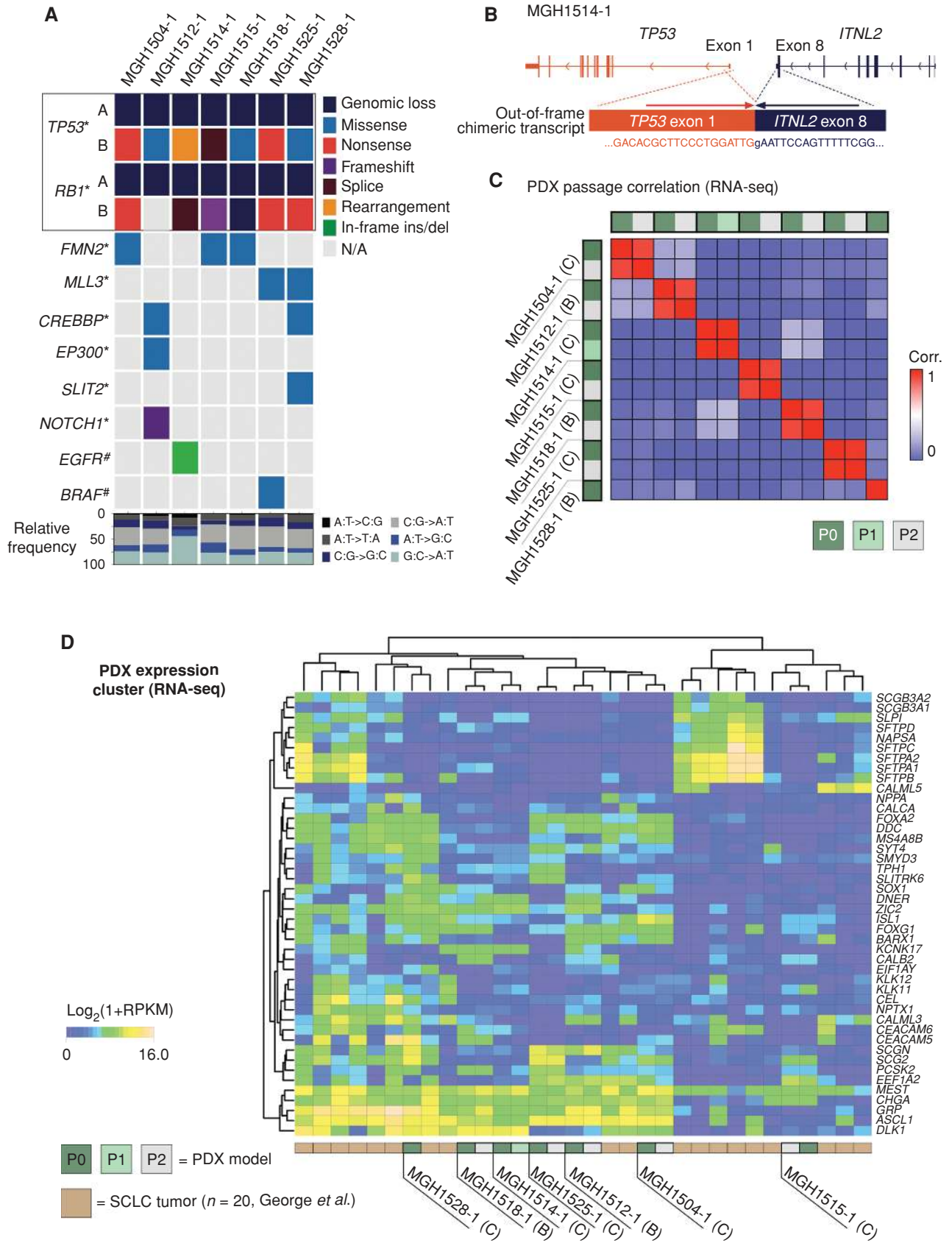
To confirm that the PDX tumors were pathologically consistent with SCLC, histologic and immunohistochemical analysis of the P0 PDX models was performed by a thoracic pathologist (M. Mino-Kenudson) and compared with the

patient biopsy when available. In all cases examined, the PDX model demonstrated histologic and immunohistochemical features consistent with SCLC, including neuroendocrine marker expression and absence of nuclear RB (representative examples are shown in Fig. 1E and Supplementary Fig. S1). Detection of CD45 was used to rule out lymphoproliferation and was negative in all 30 models tested (Fig. 1E; Supplementary Fig. S1, data not shown). Histologic comparison of PDX and corresponding patient biopsy samples showed strong similarity across the models (Supplementary Table S1).

Genomic Characterization of SCLC PDX Models

We selected seven PDX models for whole-exome sequencing (WES; Table 1) and examined the somatic alterations in these models (Supplementary Tables S3 and S4). To account for contaminating mouse tissue DNA in the PDX tumor samples, computational analyses excluded mouse reference sequencing reads (Methods). Consistent with the known genomic hallmarks of SCLC (22–24, 29, 30), WES aided in the identification of inactivating alterations of *TP53* and *RB1* in all models and confirmed biallelic loss of these tumor-suppressor genes in most cases (Fig. 2A; Supplementary Table S4). MGH1514-1 and MGH1512-1 were only found with heterozygous loss of *TP53* and *RB1*, respectively, which may be due to the technical limitations of WES in detecting larger complex genomic rearrangements that commonly affect these

Figure 2. Genomic alterations and expression profiles in SCLC PDX models. **A**, Spectrum of genomic alterations in the panel of 7 PDX models. Top plot, biallelic genomic inactivation of *TP53* and *RB1*. Bottom plot, notable alterations in PDX models beyond *TP53* and *RB1* referring to previously identified significantly mutated genes in SCLC (*; ref. 22) and to mutated cancer census genes of therapeutic relevance (#). The bottom plot displays the type of base-pair substitution referring to the representative data of PDX P0 (Supplementary Table S2). **B**, Detection of the out-of-frame fusion transcript *TP53-ITNL2* in MGH1514-1 by paired-end RNA sequencing (RNA-seq). **C**, Pearson correlation matrix for passage 0 and passage 1–2 tumors from each model, using genes with highly variable transcription levels across all samples (max RPKM > 3, coefficient of variation > 1, 1,568 transcripts). Source of each PDX model (C, CTC; B, biopsy) is indicated in parentheses next to the model number. **D**, Clustering analysis on transcriptome sequencing data of PDX models ($n = 13$ from 7 patients) and human SCLC tumors ($n = 20$, from ref. 22) selected to represent the neuroendocrine-high and -low groups as previously described. Clustering performed on genes that distinguish human primary tumors to avoid signatures associated with human immune and stromal infiltrates. All data processed with RNA-seq pipeline for human+mouse reads.



loci in SCLC. However, paired-end transcriptome sequencing of MGH1514-1 revealed an out-of-frame chimeric transcript harboring *TP53* exon 1 fused to *ITNL2* exon 8 (Fig. 2B), thus implicating biallelic genomic loss of *TP53* in this tumor. Although biallelic genomic alterations of *RBI* were not detected in MGH1512-1, this tumor had low abundance of *RBI* transcripts (Fig. 2D) and lack of RB staining in IHC (Fig. 1E), indicating a functional loss of RB1 in this tumor.

Additional alterations were found in genes encoding chromatin-modifying enzymes (e.g., *CREBBP*, *EP300*, and *MLL3*), *SLIT2*, and *NOTCH1* (Fig. 2A; Supplementary Table S4), which were previously identified as significant alterations in SCLC (22–24). Although events that augment MAP kinase pathway activity are thought to be unusual in SCLC, two models harbored alterations in this pathway (Fig. 2A): MGH1525-1 had a point mutation in the DFG motif of *BRAF* thought to activate MEK/ERK signaling (*BRAF*^{G596C}; refs. 31, 32); and MGH1514-1, which was derived from a never-smoker with *de novo* SCLC, harbored an activating *EGFR* mutation (*EGFR*^{del,exon19}). Neither case had any histologic evidence of concurrent non-SCLC. All tumors with the exception of MGH1514-1 revealed a high rate of cytosine to adenine (C:A) nucleotide transversions (Fig. 2A; Supplementary Table S3), which reflects tobacco-induced mutagenesis (33) and which is consistent with the smoking history of the patients.

To complement the genomic study of the models, transcriptome sequencing was performed to determine the expression profiles of serial passages (P0 and P2; Supplementary Table S5). In order to assess the fidelity of these expression profiles within a given model, we compared the transcripts with the highest variability across all samples to generate a correlation matrix (Fig. 2C). Paired samples from the same model correlated tightly and were uncorrelated with samples from other PDX models, which emphasize reproducible expression profiles among biological replicates from different passages of the same PDX. Although paired-end transcriptome sequencing could not be performed on the matched patient biopsies, the PDX mRNA expression profiles were mapped to a previously published database of 20 human tumors (22). Using the defining features of the dominant clusters within this dataset, six of seven PDX models showed strong similarity with the neuroendocrine-high profile, with only one PDX, MGH1515-1, clustering with the neuroendocrine-low tumors (Fig. 2D). Although the dominant PDX expression profiles mapped to primary tumor clusters, each model harbored distinct and patient-specific transcriptional signatures (Supplementary Fig. S2D). To investigate these PDX-specific features, we identified transcripts that correlated strongly with either high expression in one model or absent expression in one model, and then filtered through the Molecular Signatures Database (MSigDB V6.0) preset gene families' lists for cancer-related genes (Supplementary Fig. S2; Supplementary Table S6). Interestingly, this analysis highlighted changes in the expression in pathways known to be important in SCLC. None of the models showed high-level amplification of any *MYC* family genes, but each *MYC* family member displayed elevated expression in one specific PDX model (Supplementary Fig. S2). Although the Notch signaling pathway has been implicated in the development of SCLC (22, 34–36), transcriptome sequencing revealed model-specific

expression of *NOTCH* receptors and ligands. MGH1514-1, which harbors an activating *EGFR* mutation, is distinguished by elevated expression of *EGFR* as well as other MAP kinase pathway components including *ARAF*, *CRAF*, and *MEKK1* (Supplementary Figs. S2 and S3). Notably, *EGFR* mutations have been described in rare cases of SCLC in never-smokers (37), and SCLC transformation is an established mechanism of acquired resistance to *EGFR* tyrosine kinase inhibitors in *EGFR*-mutant non-SCLC (38–41). Thus, activated pathways and gene families vary across models, suggesting that the outcome of functional studies may greatly depend on the specific PDX model used for investigation.

Genomic Fidelity of PDX Models Compared with Patient Biopsies and Over Serial Passages

We conducted comparative genomic analyses on patient-derived biopsies versus PDX models to address three important topics: (i) the genomic fidelity of the PDX models compared with patient tumor specimens collected at the same time point, (ii) the question of whether CTC-derived models are more divergent from the primary tumor than biopsy-derived models, and (iii) the question of whether genetic drift occurs during serial passaging of SCLC tumors in NSG mice.

To address the fidelity with which the xenograft models reflect primary tumors, we compared the exomes of CTC- or biopsy-derived PDX models with patient tumor biopsies collected from the patients at the same time point (Fig. 3A). WES was performed on patient tumor biopsy tissue, xenograft tumors at passage 0 (P0), xenograft tumors at P1 or P2, and patient-matched germline DNA. Among the selected series, there were four sets of PDX tumors derived from CTCs and two sets derived from biopsies. For one of our sequenced PDX models, MGH1528-1, no corresponding patient tumor biopsy material was available (Table 1).

Comparison of copy-number alterations between patient biopsy and PDX samples demonstrated a high degree of similarity, and comparison of successive PDX passages showed few changes in copy number (Fig. 3B). Consistent with previous observations (24), the copy-number profile of most SCLC tumor models pointed to LOH or copy-neutral LOH affecting 3p, 13q (harboring *RBI*), and 17p (harboring *TP53*) as well as frequent broader chromosomal gains on 3q and 5p (Fig. 3B). Notably, MGH1514-1 did not share these canonical genomic characteristics of SCLC tumors, despite confirmed inactivation alterations of *TP53* and *RBI* (Fig. 2).

There was an approximate 10-fold range in mutational burdens across the subset of sequenced PDX models, from 27 mutations in MGH1514-1 (<1 mut/Mb) to over 500 mutations in MGH1528-1 (>10 mut/Mb; Fig. 3C). Despite this wide range, we found minimal variation in mutational burden or the distribution of mutation types between patient biopsy and PDX. There was also no significant accumulation of mutations across two PDX passages (<1%). We further analyzed the retention of individual mutations between patient biopsy and PDX models at separate passages. In 5 of the 6 cases (with the exception of MGH1514), at least 95% of all somatic alterations were shared between the tissue biopsy and PDX models (Fig. 3D; Supplementary Fig. S4). The rare differences between tissue biopsy and PDX samples included

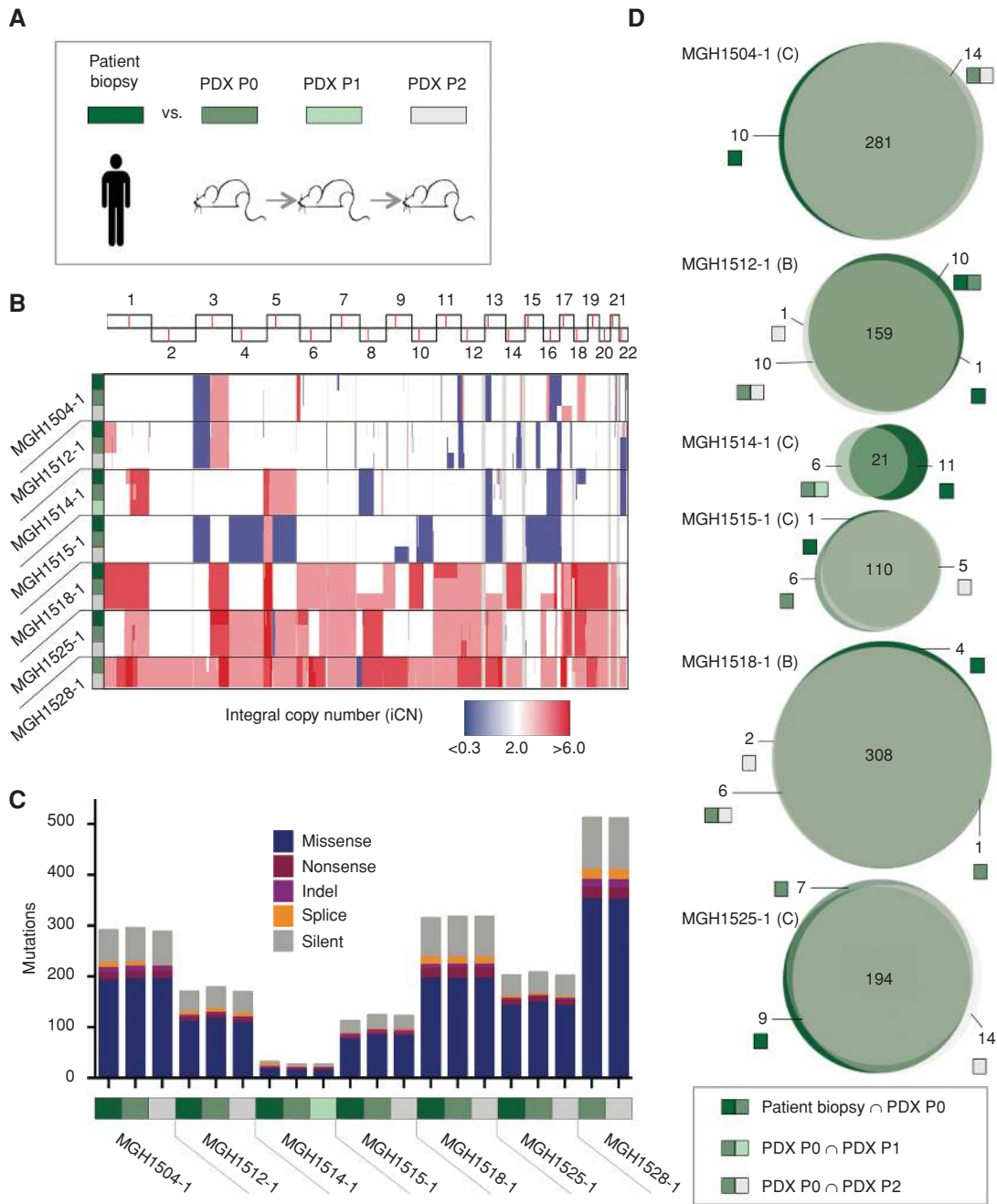


Figure 3. High genomic fidelity of SCLC PDX models derived from both CTCs and biopsies. **A**, Comparative genomic analysis on patient biopsy vs. PDX P0 and subsequently passaged PDX tumors (P1 for MGH1514-1 or P2 for all other models). **B** and **C**, Analysis of the copy-number alteration status (**B**) and of the number and type of somatic mutations (**C**) is displayed for six models. Initial tumor biopsy and derivative PDX models are described according to the color panel provided in **A**. **D**, Venn diagrams show overlap of mutations between patient biopsy, PDX P0 and PDX P1/2 exomes. Diagrams are colored according to the annotation in **A** and are scaled to total number of mutations. Number of private mutations not shared by all three samples is shown in side of the diagrams, with color bar below indicating the sample(s). Source of each PDX model (C, CTC; B, biopsy) is indicated in parentheses next to the model number.

an in-frame deletion in *MTOR*, present in the MGH1504 patient tumor biopsy but not in the CTC-derived PDX; a heterozygous *PIK3CA* splice-site mutation acquired in the MGH1514-1 PDX model; and single-copy gain of the *MYCL1* locus in the MGH1515-1 PDX that may be reflected in the increased transcript levels (Fig. 2D; Supplementary Table S5). The fraction of shared mutations between PDX P0 and the

patient biopsy was not significantly different from the fraction shared between P0 and subsequent passages. This held true for both biopsy- and CTC-derived models, indicating that the CTCs collected at the time of the biopsy share the same genomic features as the sampled solid tumor. This result is consistent with the low degree of clonal heterogeneity in SCLC that has been previously reported (22). In summary, SCLC PDX

Downloaded from <http://aacrjournals.org/cancerdiscovery/article-pdf/8/5/600/1839874/600.pdf> by guest on 27 August 2022

models retain a stable genome and maintain their somatic alterations between initial model generation (P0) and serial passages (P1/P2; >95%), thus faithfully recapitulating SCLC patient tumors at the time of model generation.

Functional Fidelity of PDX Models to Patient Response to Chemotherapy

To further assess the capacity of the PDXs to accurately model characteristics of the patient tumor, we sought to quantify their responses to EP. Acquired resistance to EP is commonly observed in the clinic. However, there was no correlation between patient treatment histories and sensitivity to chemotherapeutics *in vitro* across a panel of 63 human SCLC cell lines (42), suggesting inadequacy of the cell lines for modeling clinical behavior. PDXs may better recapitulate patient treatment histories.

To assess EP response in our models, we first optimized an EP regimen to distinguish between serial PDX models derived from the same patient (MGH1518) prior to first-line chemotherapy and after subsequent lines of therapy (Fig. 4A and B). This regimen consists of cisplatin 7 mg/kg intraperitoneal (i.p.) day (d)1 and d8 plus etoposide 10 mg/kg i.p. d1, d2, d3, and d8, d9, d10. Significant tumor shrinkage was induced in the EP-naïve model, but not the model derived after the patient had received prior EP, recapitulating the evolving resistance of the patient's tumor (Fig. 4B).

We then applied this EP dosing strategy to 30 PDX models, including 12 treatment-naïve models and 18 post-relapse models (Fig. 4C; Supplementary Fig. S5). Using large numbers of mice for each model would limit the feasibility of a population-based approach, and recent studies of hematopoietic and solid-tumor PDX model populations have shown that small numbers of animals are sufficient to accurately compare tumor responses (43, 44). Models were therefore treated in biological duplicate or triplicate, and consistent with these studies, our results show highly concordant tumor volume curves between different mice carrying the same PDX (Fig. 4B; Supplementary Fig. S5). Responses were quantified by measuring the maximum depth of tumor response [minimum percent initial tumor volume (ITV) in the days 14–28 window of the treatment], as well as the time to progression (TTP; days to 2x ITV; Fig. 4A). Response and TTP were strongly correlated across the model panel (Fig. 4D), and these metrics were applied to assess the fidelity of the models to patient responses.

To determine whether prior patient exposure to chemotherapy correlated with EP sensitivity in the models, the metrics of PDX response were compared between models derived from EP-naïve versus EP-treated patients (Fig. 4E). Maximum tumor response was significantly different, with nearly uniform sensitivity of models from EP-naïve patients and a range of responses in the models from previously treated patients (Fig. 4F). Clinically, first-line chemotherapy is administered for a finite number of cycles, as opposed to ongoing administration until resistance emerges. Therefore, this range of responses in post-relapse models is expected. When we examined TTP as a metric of model sensitivity to EP, we observed a trend toward prolonged TTP in the models from treatment-naïve patients compared with models from previously treated patients (Supplementary Fig. S6). Notably,

assessment of xenograft TTP can be complicated by differences in intrinsic xenograft doubling times (Supplementary Fig. S7). To correct for this, the doubling times of each model (T_{dbl}) were calculated for each model in untreated xenografts. Doubling times were uncorrelated with patient treatment history (Fig. 4G; Supplementary Fig. S8). The corrected TTP [calculated as the ratio of TTP (doubling time in the presence of EP) to intrinsic doubling time; TTP/T_{dbl} ratio] was significantly different between models derived from EP-naïve versus EP-treated patients (Fig. 4H; Supplementary Fig. S8).

We next sought to assess whether the relative TTP of each PDX model was consistent with the TTP of its donor patient. Patient TTP was measured as the number of days from the last dose of EP to the date of first radiographic progression of disease. Although many variables can affect TTP in the clinic, we found that the model EP response was moderately correlated with patient TTP among PDXs derived from previously treated patients (Fig. 4I). This is consistent with the clinical observation that TTP following EP correlates with likelihood of response to next-line DNA-damaging therapy (45). Clinical TTP data for models from EP-naïve patients were limited to a smaller number of cases, and as a result, a thorough comparison to model TTP could not be performed.

Collectively, these results show that PDX responses and TTPs correlate with the patient treatment histories. These results stand in contrast to results from established cell lines, where chemotherapy sensitivity is uncorrelated with patient treatment history (42), and suggest that PDXs more accurately model the clinical behavior of these cancers. Importantly, they also support the application of PDXs for studying clinically relevant EP resistance, acquired in patients rather than in an experimental laboratory system.

We therefore next sought to identify potential molecular features that correlate with chemoresistance. Transcriptome sequencing was performed on a subset of 19 models treated with EP and analyzed for signatures that correlated with treatment sensitivity versus resistance (Supplementary Table S7). In parallel, quantitative Western blots for selected proteins with potential impact on chemoresistance were performed across the 30-model EP cohort. Transcript and protein levels were closely matched for most models in which both could be compared (Fig. 4J; Supplementary Fig. S9).

Recently, the putative RNA–DNA helicase *SLFN11* has been associated with sensitivity to a number of DNA-damaging therapies, including EP (42, 46). In our PDX cohort, neither *SLFN11* transcript levels (19 models) nor protein levels (30 models) correlated with EP response or TTP (Fig. 4K; Supplementary Fig. S9). Furthermore, *SLFN11* levels were approximately equivalent in models derived from treatment-naïve and previously treated patients (Fig. 4L; Supplementary Fig. S9). A similar lack of correlation with EP response was observed for *ASCL1* and *NEUROD1* (Supplementary Fig. S9).

A systematic analysis of the transcriptome sequencing dataset was performed to identify features and pathways that best correlated with EP response (Supplementary Fig. S10). The best-correlated transcripts (absolute Spearman coefficient >0.6, 359 genes) were analyzed by gene set enrichment analysis (GSEA; MSigDB v6.0) using only the Hallmark gene sets, a curated collection with small numbers of elements in each set, compiled from multiple independent databases (47,

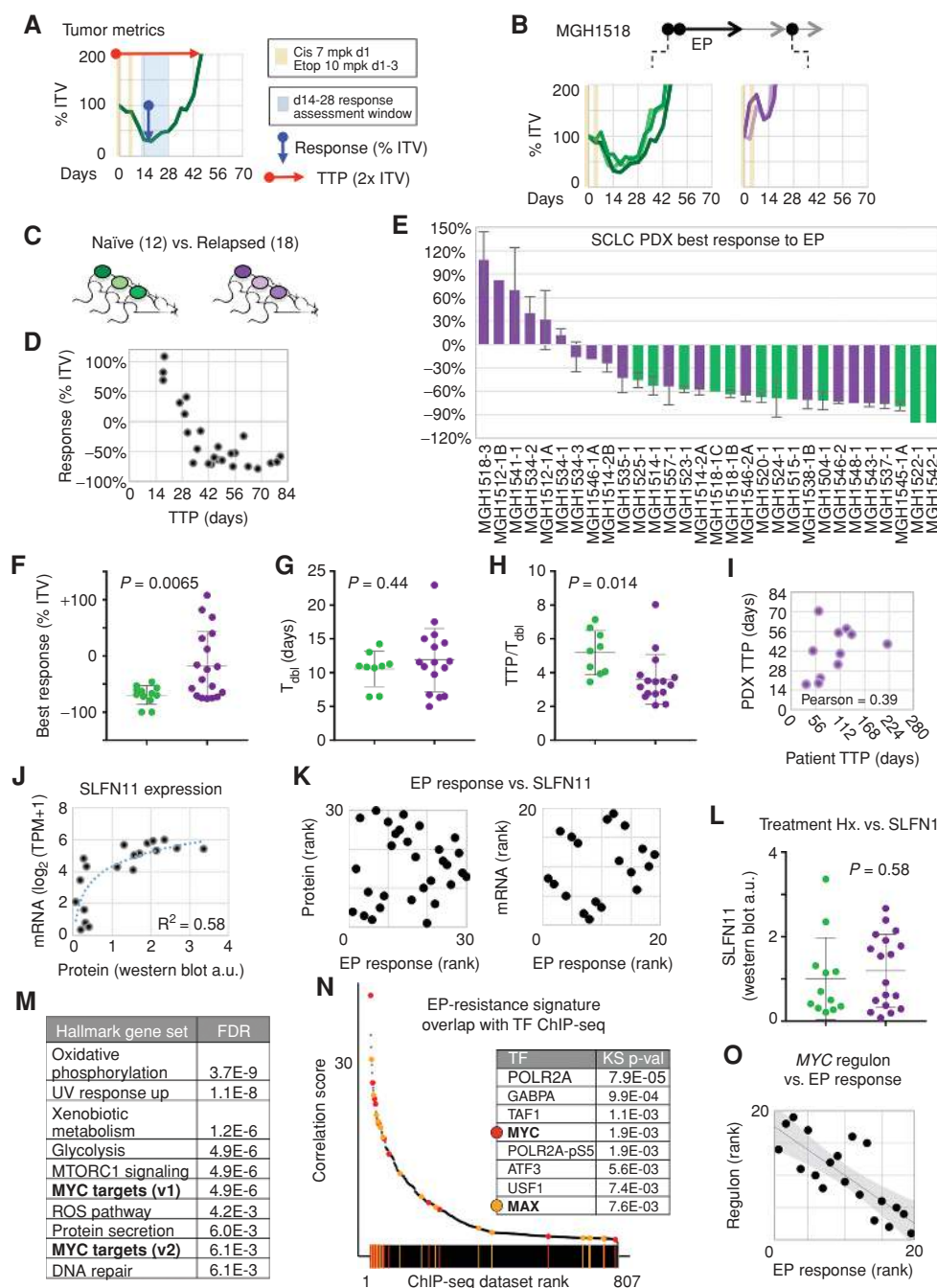


Figure 4. SCLC PDX model responses to first-line chemotherapy reflect patient treatment histories. **A**, % ITV vs. days after EP start for a single xenograft treated with two 1-week cycles of cisplatin 7 mpk i.p. d1 + etoposide 10 mpk i.p. d1-3 (tan bars). Response = minimum %ITV between d14 and d28. TTP = time to 2x ITV. **B**, Differential EP response of serial models from patient MGH1518 derived before first-line chemotherapy and after second-line therapy. **C**, Trial of EP across a population of 30 PDX models: 12 from treatment-naïve patients (green) and 18 from previously treated patients (purple). Results presented in **D-O**, with same green/purple color code in **E-I** and **L**. **D**, Correlation of PDX EP response and TTP. **E**, Waterfall plot of PDX best response. **F-H**, Comparison of tumor metrics following EP treatment in PDX models from treatment-naïve vs. post-relapse patients, with unpaired *t* test *P* values: best response (**F**), doubling time (**G**), and ratio of TTP to doubling time (**H**). **I**, TTP in post-relapse PDX models vs. EP TTP in the donor patients. **J**, Correlation of SLFN11 transcript abundance in transcriptome sequencing (TPM), and protein levels measured by quantitative Western blot (arbitrary units) across 19 models, with logarithmic trend line. **K**, Lack of correlation between EP response (rank 1 = deepest response) and SLFN11 expression (rank 1 = highest level): protein on left (30 models), transcript on right (19 models). **L**, No difference in SLFN11 protein levels between PDX models from treatment-naïve vs. post-relapse patients. **M**, Gene set enrichment analysis (GSEA) of transcripts that correlate with PDX EP resistance (Spearman $\rho > 0.6$) using “Hallmark” gene sets (MSigDB v6.0). Gene sets with FDR of less than 1% are shown. **N**, 200 putative MYC targets that correlate with GSEA MYC signature were compared with inventory of chromatin immunoprecipitation sequencing (ChIP-seq) datasets. A total of 807 datasets from ENCODE, covering 181 transcription factors (TF), had >1 intersecting gene. Inset: top enriched TFs for these genes, with a Kolmogorov-Smirnov (KS) statistic *P* value < 0.01. **O**, MYC regulon correlates with EP resistance. MYC regulon = 155/200 putative MYC targets that were present in top 7 MYC/MAX ChIP-seq dataset. Regulon expression rank vs. EP response rank for 19 PDX models.

Downloaded from <http://aacrjournals.org/cancerdiscovery/article-pdf/8/5/600/1839874/600.pdf> by guest on 27 August 2022

48). No gene sets were positively correlated with sensitivity to EP (FDR q -value cutoff <0.01), reflecting the high stringency of the analysis. However, 10 gene sets scored for EP resistance, including genes upregulated in response to UV and reactive oxygen species exposure, and genes involved in drug detoxification (“xenobiotic metabolism”; Fig. 4M; Supplementary Table S8).

Also among these were two distinct *MYC* target lists containing 14 genes in total, which we term the “small *MYC*” regulon. A *MYC* target signature was of particular interest given recent data that overexpression of *Myc* in an SCLC GEMM promotes tumor growth and may confer relative chemotherapy resistance (49). Given the number of potential *MYC* targets that contain a canonical E-box, we performed a secondary assessment of whether these 14 genes represented a *MYC* transcription signature. We identified the 200 transcripts that most closely mirrored the expression pattern of the small *MYC* regulon. These transcripts were compared by enrichment analysis (Enrichr) with the ENCODE collection of transcription factor chromatin immunoprecipitation sequencing (ChIP-seq) datasets (50, 51). A total of 807 ChIP-seq datasets from 181 transcription factors contained at least 1 overlapping gene with the query set (Fig. 4N; Supplementary Table S8). *MYC* and *MAX* ChIP-seq datasets were among the most enriched for the 200-gene query set, as well as the *MYC* family transcription factor *USFI*, supporting the conclusion that the 14-gene signal initially detected by GSEA does represent a *MYC* target signature (Fig. 4M). Indeed, 155 of 200 genes in the large *MYC* set were contained within the top 8 ChIP-seq datasets (Supplementary Table S8). This “large *MYC*” regulon, composed of E-box-containing genes that are directly bound by *MYC*, was strongly anticorrelated with EP sensitivity, measured by both response and TTP (Fig. 4P; Supplementary Fig. S11). These results support the conclusion that upregulation of a *MYC* signature may be a biomarker of EP resistance. Furthermore, this analysis demonstrates that this large panel of PDX models and their quantified EP sensitivities can be applied for novel discovery of transcriptional profiles correlated to chemotherapy sensitivity or resistance.

Correlation between Patient and Model Responses to an Experimental Therapy

To address the capacity of serial PDXs to model tumor evolution from a single patient over multiple time points, we focused on models derived from MGH1528. The patient was a 58-year-old male who had received several prior lines of therapy (MGH1528, Table 1). He was enrolled onto an ongoing phase I/II clinical trial of combination olaparib and temozolomide (OT) in patients with SCLC that has progressed following at least one prior line of chemotherapy (NCT02446704). At the time of enrollment on the clinical trial, the patient had widely metastatic disease including a large left axillary mass (Fig. 5A). He was treated with OT and had a partial response by RECIST 1.1 criteria, with a nadir at day 89. He remained on study 6.5 months, but ultimately developed progressive disease.

Serial PDX models were generated from CTCs immediately prior to enrollment onto the OT trial (MGH1528-1) and at the time of relapse (MGH1528-2), which allowed for pharmacologic interrogation *in vivo* with the mouse model and

in vitro with PDX-derived short-term cell cultures (STC; Fig. 5B and C). We first assessed the *in vivo* response of the tumors to the combination treatment with OT. Mice bearing tumors from MGH1528-1 were treated with one cycle of OT, which resulted in dramatic tumor regressions, whereas tumors in vehicle-treated mice progressed rapidly (Fig. 5B). However, the PDX tumors derived after the patient’s progression on OT (MGH1528-2) did not respond to this treatment and in fact demonstrated similar growth kinetics to the vehicle-treated animals (Fig. 5B). These serial CTC-derived PDX models therefore reflected the evolving treatment sensitivities of the patient tumor at the time of CTC collection.

Although PDX models permit functional analysis of patient drug responses, the requirement for *in vivo* experiments may limit both throughput and assay variety. STCs could greatly expand the range of analyses of PDX models while generating fewer *in vitro* artifacts than long-term cell line establishment. STCs were initiated from the MGH1528 serial models and treated with two-dimensional titrated combinations of olaparib and temozolomide (Fig. 5C). Cultures were initiated on the day of tumor resection and treated within 24 hours of cell seeding. The MGH1528-1 culture demonstrated high sensitivity to both olaparib and temozolomide, as well as the combination. By contrast, MGH1528-2 was significantly less sensitive to the OT combination (Fig. 5C). Thus, OT responses in STCs derived from serial PDX models show concordance with both *in vivo* responses and the patient clinical course. We anticipate that these types of serial models will enable detailed mechanistic studies of how resistance to therapy evolves in patients.

DISCUSSION

Numerous model systems for studying SCLC exist, including cell lines, GEMMs, and PDXs. Although each has its relative merits and limitations, the purpose of any model system is to enable clinically relevant and impactful discoveries. Here, we report the efficient production of a large panel of PDX models and demonstrate the high genomic and functional fidelity of these models when compared with the patient tumors from which they were derived. These findings support a prominent role for PDX models in SCLC translational science. The high efficiency of our PDX development platform (38% for CTCs and 89% for biopsies) suggests that the generation of large model populations, as well as serial models from the same patient, may ultimately become routine, particularly in the context of clinical trials.

Importantly, our experience generating SCLC PDXs from biopsies and effusions demonstrates that model development is highly efficient from a wide variety of metastatic sites (including lymph nodes, subcutaneous nodules, brain metastases, adrenal metastases, and pleural fluid) and using a variety of modalities (including CT-guided biopsy, ultrasound guided biopsy, endobronchial ultrasound, surgical resection, thoracentesis, and pericardiocentesis; Supplementary Table S2). PDX development was more efficient from biopsies than from CTCs, likely due to larger numbers of starting tumor cells and preservation of tumor microenvironments. At Massachusetts General Hospital (MGH), core biopsies at the time of diagnosis are standard, even for suspected SCLC. This

The CTC-iChip or similar automated technologies may further help to standardize the generation of SCLC PDX models, particularly in situations when a biopsy is not otherwise clinically indicated. In addition to our own technology, there are multiple similar technologies currently available including Clearbridge, Apocell, and CytoScale (reviewed in ref. 21). The CTC-iChip technology is also currently being commercially developed. We anticipate that the high efficiency of PDX generation from CTCs will be reproducible with other microfluidic CTC isolation technologies, though this remains to be directly tested.

SCLC tumors have extremely complex genomes with extensive copy-number alterations and a high mutational burden. Furthermore, these tumors harbor recurrent alterations that can promote genome instability, most notably inactivation of *TP53* and *RBI1*. Initial studies on PDX models of SCLC have confirmed that they share the genomic and molecular hallmarks of the human disease (5, 10, 15). However, the extent to which an individual model faithfully recapitulates the specific molecular and functional characteristics of the donor patient tumor has been uncertain.

Here, we performed a comprehensive genomic study of SCLC PDX models, which for the first time demonstrates that the somatic mutational landscapes of the models closely match synchronous tumor biopsies and remain stable over early passages in mice. These features are true of both biopsy- and CTC-derived PDX models and stand in contrast to other solid tumor types. For malignancies such as lung adenocarcinoma (52), colorectal cancer, and melanoma (53, 54), marked genomic heterogeneity has been observed between anatomically distinct metastases, especially following the emergence of resistance to therapy. For PDX models of breast cancer, retention of intratumor heterogeneity has been demonstrated, as well as the evolution of new subclones over serial passages (55). Furthermore, a recent comprehensive study of PDX models derived from diverse tumor types, but excluding SCLC, demonstrated marked genomic evolution over early passages (25). Therefore, the fidelity of the CTC-derived SCLC models was particularly surprising: A small number of tumor cells with high mutational burdens, shed into circulation, collected, grown into xenografts, and repeatedly passaged, were found to have nearly superimposable genomes with patient tumor biopsies taken from anatomically distinct locations (Fig. 3D). This supports the idea that despite a high mutational burden (>8 mutations per Mb), clonal homogeneity is a distinguishing feature of SCLC (22) and, in addition, suggests relative genomic stability. The genomic fidelity of CTC-derived models has important implications for the utility of SCLC CTCs in translational research, and for the validity of molecular diagnostics that use live cells and cell-free DNA. We do note that there are handful of somatic alterations that differ between the PDX models and the biopsies (<5%). It remains to be understood how these subtle differences affect the functional fidelity of the PDX to the patient's tumor, and further assessments of SCLC PDX models are undoubtedly warranted.

A large panel of PDX models, derived from both treatment-naïve and previously treated patients, enables well-powered functional *in vivo* studies. Here, among 30 PDX models, we observe a range of sensitivities to standard-of-care chemotherapy, EP. Unlike in SCLC cell lines (42), EP sensitivity in our PDX models correlates with patient treatment history, supporting the conclusion that these models more accurately

recapitulate the behavior of patients' tumors. The breadth of this collection of PDXs also enables analysis of correlative transcription signatures. Across 19 models, we identify several expression signatures that correlated with relative EP resistance, many of which warrant further study. Notably among this list, we observe that expression of a subset of *MYC* targets emerges as a marker of EP resistance. This observation is consistent with recent work in GEMMs, where overexpression of *Myc* promotes growth of tumors that rapidly relapse after EP treatment *in vivo* (49). In GEMMs, *Myc* overexpression drives a *Neurod1*-high, *Ascl1*-low (so-called "neuroendocrine-low") profile, though this dichotomy is less prominent across a panel of human cell lines and tumors. Similarly, we find that some tumors exhibit distinct expression of these two transcription factors (Supplementary Fig. S9A), though others do not fit this pattern of mutually exclusive expression. Thus, although the interplay between expression of *MYC*, *NEUROD1*, and *ASCL1* may be more complex in human tumors than in GEMMs, our findings support the conclusion that a *MYC* expression signature is a marker of greater chemotherapy resistance in SCLC, and we provide a demonstration of this observation in unperturbed samples from patients.

SLFN11 has also been described as a potential biomarker of sensitivity to DNA-damaging agents (5, 10, 46, 56). In a study by Gardner and colleagues, acquired EP resistance in PDX models derived from chemotherapy-naïve patients led to downregulation of *SLFN11*. By contrast, we found *SLFN11* expression levels (mRNA or protein) did not correlate with either PDX EP response or history of prior chemotherapy exposure for the donor patients. These differences likely arise from the fact that these are orthogonal experiments: one testing the effect of induced high-level EP resistance within the same model and the other comparing expression with intrinsic chemotherapy response and clinical history. Additional work is warranted to elucidate the role of *SLFN11* and its potential applications, but in our dataset, it was not a biomarker of EP sensitivity.

In summary, we introduce here a new strategy for efficient development of a panel of SCLC PDX models, validate the genomic and functional fidelity of these models, and use the panel to assess markers of chemotherapy response. We believe that these advances lay the foundation for further functional analyses across large panels of SCLC PDX models in which experimental results can be directly compared with patient clinical outcomes. In addition, reliably efficient generation of PDX models enables generation of isogenic models from patients with SCLC at multiple times in their treatment course. We anticipate that these types of models will be a powerful resource in the context of SCLC drug development, facilitating the identification of biomarkers and mediators of sensitivity and acquired resistance to therapy.

METHODS

Extended methods are available in Supplementary Materials.

PDX Model Generation

All tissue and blood samples from patients were collected per IRB-approved protocols with written informed consent from the patients and in accordance with the Declaration of Helsinki. All mouse studies were conducted through Institutional Animal Care and Use

Committee-approved animal protocols in accordance with MGH institutional guidelines. To initiate a PDX model (P0), SCLC tumor material (CTCs, leukocyte/RBC-depleted effusion, or tumor core needle biopsy or surgical sample) was resuspended in 1:1 ice-cold HITES media and Matrigel (Corning), and injected subcutaneously via large bore (18G) needle into the right flank of an NSG mouse (NOD.Cg-Prkdc^{scid} Il2rg^{tm1Wjl/Szj}; Jackson Laboratories). Whole blood and pleural or pericardial effusions were collected and transported at room temperature, and core biopsy samples on ice. Biopsy samples were diced by scalpel prior to resuspension and injection. Effusion samples were red blood cell (RBC)-depleted (BioLegend RBC lysis buffer) and leukocyte depleted (Miltenyi Biotec anti-CD45 IgG microbeads) per standard protocols. SCLC CTCs were enriched from fresh peripheral blood samples using either the CTC-iChip microfluidic device, as described previously for negative depletion of leukocytes and enrichment of untagged CTCs (27, 28), or the manual Ficoll gradient method previously described (20). After tumor emergence, palpable tumors were measured with electronic calipers weekly until tumors exceeded 1,500 mm³, at which point animals were euthanized and tumors were resected. Scalpel-dissected xenograft fragments were either immediately implanted into NSG mice for passaging, cryopreserved for later passaging, fixed in 10% neutral buffered formalin (Sigma) for pathologic analysis, or fresh-frozen in liquid nitrogen for molecular analysis. For pathologic review, 5 μm sections of formalin-fixed, paraffin-embedded (FFPE) tissue were stained with hematoxylin and eosin as well as antibodies against chromogranin, synaptophysin, CD56, CD45, and RB (antibody details in Supplementary Methods). The histologic diagnosis of small cell carcinoma was rendered in accordance with World Health Organization Classification of the Lung, Pleura, Thymus and Heart, 4th edition (57).

WES and Transcriptome Sequencing

Total DNA and RNA were isolated from fresh-frozen or FFPE tumor tissue, and germline DNA was obtained from matched normal donor blood or FFPE tissue histologically confirmed to be free of tumor cells. DNA from FFPE tissue was extracted with the Maxwell FFPE DNA Purification Kit on a Maxwell 16 MDx instrument (Promega). Nucleic acids were extracted from fresh-frozen tissue and patient-derived blood by standard protocols (Supplementary Methods). For WES, DNA was fragmented by sonication, end-repaired, and adaptor ligated with incorporation of index barcodes, size-selected and enriched with Sure select XT (Agilent), and sequenced with a paired-end 2 × 75 bp protocol for an average coverage of 100–120× (Supplementary Table S3). For paired-end RNA sequencing (RNA-seq), cDNA libraries were prepared with the Illumina TruSeq kit and sequenced with a paired-end 2 × 75 bp protocol on an Illumina HiSeq instrument. For single-end RNA-seq, cDNA libraries were prepared with the Kapa Stranded RNA-seq Kit with Ribotase HMR method and sequenced with a single-end 75 bp protocol on a NextSeq 500 instrument. Sequence alignments were performed against both human and mouse reference genomes to filter mouse-specific reads. Somatic mutations and copy-number alterations were determined as previously described (22, 24). Transcript expression levels were determined using Cufflinks and expressed as reads per kilobase million (RPKM; paired-end RNA-seq) or using Kallisto and expressed as transcripts per million (TPM; single-end RNA-seq). Downstream bioinformatic analyses are described in the Supplementary Information. Paired-end whole-exome and transcriptome sequencing data are deposited at the European Genome-phenome Archive, which is hosted by the EBI (EGA; <http://www.ebi.ac.uk/ega/>), under accession number EGAS00001002853. Single-end transcriptome sequencing data are deposited in the NCBI's Gene Expression Omnibus (GEO; <https://www.ncbi.nlm.nih.gov/geo/>), under accession number GSE110853.

Immunoblotting

Fresh-frozen xenograft samples were lysed in RIPA buffer using a TissueLyzer II (Qiagen) homogenizer. SDS-PAGE was performed by

standard methods, and PVDF membranes were probed with the following antibodies: from Cell Signaling Technology: alpha-tubulin, beta-actin, NeuroD1, total EGFR, pAKT (S473), pERK1/2 (T202/Y204); from Abcam: Ascl1 (MASH1); from Santa Cruz Biotechnology: Slfn11. Membranes were imaged with a Syngene G:BOX, and band densitometry was performed using Syngene GeneSys software. Ratio to loading control (alpha-tubulin) was calculated, and lysates from established SCLC cell lines (CORL88, CORL279, NCIH82, NCIH1048, and DMS273) were used as interblot standards. Cell lines were obtained between 2015 and 2017 from the MGH Center for Molecular Therapeutics, which performs routine authentication by single-nucleotide polymorphism and short tandem repeat analyses, and were passaged in HITES media + 2% FBS for less than 3 months prior to lysate preparation.

Mouse Treatment Studies

Trials were initiated at xenograft volumes of 400 to 600 mm³ for 3 to 5 mice per model per treatment arm, and tumors were measured 2 to 3x weekly. EP: cisplatin 7 mg/kg i.p. d1,8 + etoposide 10 mg/kg i.p. d1-3,8-10. OT: olaparib 50 mg/kg oral gavage (OG) d1-5 + temozolomide 25 mg/kg OG d1-5. EP trial tumor metrics: TTP = days from start of treatment to 2x ITV, response = change in tumor volume between ITV and d14–28 minimum, TTP/T_{dbl} = ratio of TTP to tumor doubling time in untreated mice. Endpoints: tumor volume > 2x ITV or 80 days after start of treatment.

PDX Short-Term Cultures

Xenografts were resected, fragmented, and rapidly dissociated with a gentleMACS Octo Dissociator (Miltenyi Biotec). Live cells were enriched by Ficoll gradient and depleted of murine cells with anti-mouse IgG microbeads (Miltenyi Biotec). PDX culture suspension was seeded in 96-well format in HITES media + 2% FBS + 10 μmol/L ROC kinase inhibitor (Y-27632; Selleckchem). Titration of olaparib and temozolomide was performed with a D300e digital drug dispenser (Tecan Life Sciences). Viability was assessed after 5 days using CellTiter-Glo (Promega).

Disclosure of Potential Conflicts of Interest

B.J. Drapkin reports receiving commercial research support from Novartis. M. Mino-Kenudson is a consultant/advisory board member for H3 Biomedicine and Merrimack Pharmaceuticals. S. Lakis is a consultant/advisory board member for BioNTech Diagnostics. R.S. Heist is a consultant/advisory board member for Boehringer Ingelheim. R. Büttner is a consultant/advisory board member for AbbVie. L.V. Sequist is a consultant/advisory board member for AstraZeneca, Boehringer Ingelheim, Genentech, Merrimack, Novartis, and Pfizer. A.N. Hata reports receiving commercial research grants from Amgen, Novartis, and Relay Therapeutics. S. Maheswaran has applied for patent protection for the CTC isolation technology. D.A. Haber has applied for patent protection for the CTC isolation technology. N. Dyson reports receiving commercial research support from Novartis. R.K. Thomas reports receiving a commercial research grant from Roche; has received honoraria from the speakers bureaus of AstraZeneca, Boehringer Ingelheim, Clovis, Daiichi-Sankyo, Lilly, Merck, MSD, Puma, and Roche; and is a consultant/advisory board member for Neo New Oncology GmbH. A.F. Farago reports receiving commercial research support from AbbVie, AstraZeneca, Novartis, PharmaMar, Loxo Oncology, Ignyta, Merck, and Bristol-Myers Squibb; has received honoraria from the speakers bureau of Foundation Medicine; and is a consultant/advisory board member for AbbVie, PharmaMar, Loxo, Takeda, and Merrimack. No potential conflicts of interest were disclosed by the other authors.

Authors' Contributions

Conception and design: B.J. Drapkin, S. Maheswaran, N. Dyson, A.F. Farago

Development of methodology: B.J. Drapkin, J. George, R. Büttner, L.V. Sequist, A.N. Hata, M. Toner, S. Maheswaran, M. Peifer, R.K. Thomas, A.F. Farago

Acquisition of data (provided animals, acquired and managed patients, provided facilities, etc.): B.J. Drapkin, J. George, C.L. Christensen, M. Mino-Kenudson, T. Sundaresan, S. Phat, D.T. Myers, J. Zhong, P. Igo, M.H. Hazar-Rethinam, J.A. Licausi, K.N. Jani, R. Menon, R.S. Heist, R. Büttner, K.-K. Wong, A.N. Hata, D.A. Haber, R.K. Thomas, A.F. Farago

Analysis and interpretation of data (e.g., statistical analysis, biostatistics, computational analysis): B.J. Drapkin, J. George, C.L. Christensen, M. Mino-Kenudson, R. Dries, T. Sundaresan, M.H. Hazar-Rethinam, N. Abedpour, R. Menon, S. Lakis, R.S. Heist, R. Büttner, S. Haas, A.T. Shaw, K.-K. Wong, A.N. Hata, S. Maheswaran, M. Peifer, R.K. Thomas, A.F. Farago

Writing, review, and/or revision of the manuscript: B.J. Drapkin, J. George, M. Mino-Kenudson, R. Dries, T. Sundaresan, S. Lakis, R.S. Heist, L.V. Sequist, A.T. Shaw, A.N. Hata, S. Maheswaran, M. Peifer, N. Dyson, R.K. Thomas, A.F. Farago

Administrative, technical, or material support (i.e., reporting or organizing data, constructing databases): B.J. Drapkin, J. Zhong, M. Gomez-Caraballo, M. Kem, R. Azimi, M. Toner, S. Maheswaran, D.A. Haber, R.K. Thomas, A.F. Farago

Study supervision: B.J. Drapkin, J. George, S. Maheswaran, N. Dyson, R.K. Thomas, A.F. Farago

Acknowledgments

We are grateful to the patients and families who participated in these research studies. We thank Jeffrey Engelman for his vision and guidance in launching this project. We thank M. Stanzione, I. Sanidas, A. Guarner-Peralta, B. Krishnan, K. Tschop, W. Miles, B. Nicolay, and current and former members of the Dyson and Farago research groups; L. Zou, R. Corcoran, and C. Benes for critical discussions and scientific input; and J. Sullivan for guidance on CTC isolation. We thank the regional computing center of the University of Cologne (RRZK) for providing the CPU time on the DFG-funded supercomputer “CHEOPS” as well as the support. We thank the members of the MGH thoracic oncology group and other MGH Cancer Center staff for assistance with recruitment of patients and collection of samples. This work was supported by the V foundation for Cancer Research (T2016-003, to N. Dyson and A.F. Farago), a grant from Uniting Against Lung Cancer: New England (UALC2014, to A.F. Farago), Conquer Cancer Foundation of ASCO Young Investigator Awards (YIA 2014, to A.F. Farago; YIA 2017, to B.J. Drapkin), the President and Fellows of Harvard College (CMeRIT, to A.F. Farago), the National Institutes of Health and National Cancer Institute (Chabner K12CA087723, to A.F. Farago; Rudin U24CA213274, to A.F. Farago; K99CA201618, to C.L. Christensen; 1U01CA213333-01, to K.-K. Wong; NCI 2RO1CA129933, to D.A. Haber; NIH Quantum 2UO1EB012493, to M. Toner and D.A. Haber), the Bridge Project—a collaboration between The Koch Institute for Integrative Cancer Research at MIT and the Dana-Farber/Harvard Cancer Center (DF/HCC; to K.-K. Wong), Howard Hughes Medical Institute (to D.A. Haber), National Foundation for Cancer Research (to D.A. Haber), the German Ministry of Science and Education (BMBF) as part of the e:Med program (grant no. 01ZX1303A, to R.K. Thomas, R. Büttner, and M. Peifer; grant no. 01ZX1406, to M. Peifer), the Deutsche Forschungsgemeinschaft (DFG; through TH1386/3-1, to R.K. Thomas, and CRU-286, to M. Peifer), the Deutsche Krebshilfe as part of the Oncology Centers of Excellence funding program (to R.K. Thomas), the German Cancer Consortium (DKTK) Joint Funding program, and the International Association for the Study of Lung Cancer (IASLC Young Investigator Award, to J. George).

The costs of publication of this article were defrayed in part by the payment of page charges. This article must therefore be hereby

marked *advertisement* in accordance with 18 U.S.C. Section 1734 solely to indicate this fact.

Received August 22, 2017; revised February 12, 2018; accepted February 21, 2018; published first February 26, 2018.

REFERENCES

- Pietanza MC, Byers LA, Minna JD, Rudin CM. Small cell lung cancer: will recent progress lead to improved outcomes? *Clin Cancer Res* 2015;21:2244–55.
- Jalal SI, Lavin P, Lo G, Lebel F, Einhorn L. Carboplatin and etoposide with or without palifosfamide in untreated extensive-stage small-cell lung cancer: a multicenter, adaptive, randomized phase III study (MATISSE). *J Clin Oncol* 2017;35:2619–23.
- Tiseo M, Boni L, Ambrosio F, Camerini A, Baldini E, Cinieri S, et al. Italian, multicenter, phase III, randomized study of cisplatin plus etoposide with or without bevacizumab as first-line treatment in extensive-disease small-cell lung cancer: the GOIRC-AIFA FARM6P-MFJM Trial. *J Clin Oncol* 2017;35:1281–7.
- Reck M, Luft A, Szczesna A, Havel L, Kim SW, Akerley W, et al. Phase III randomized trial of ipilimumab plus etoposide and platinum versus placebo plus etoposide and platinum in extensive-stage small-cell lung cancer. *J Clin Oncol* 2016;34:3740–8.
- Gardner EE, Lok BH, Schneeberger VE, Desmeules P, Miles LA, Arnold PK, et al. Chemosensitive relapse in small cell lung cancer proceeds through an EZH2-SLFN11 axis. *Cancer Cell* 2017;31:286–99.
- Gardner EE, Connis N, Poirier JT, Cope L, Dobromilskaya I, Gallia GL, et al. Rapamycin rescues ABT-737 efficacy in small cell lung cancer. *Cancer Res* 2014;74:2846–56.
- Faber AC, Farago AF, Costa C, Dastur A, Gomez-Caraballo M, Robbins R, et al. Assessment of ABT-263 activity across a cancer cell line collection leads to a potent combination therapy for small-cell lung cancer. *Proc Natl Acad Sci U S A* 2015;112:E1288–96.
- Byers LA, Wang J, Nilsson MB, Fujimoto J, Saintigny P, Yordy J, et al. Proteomic profiling identifies dysregulated pathways in small cell lung cancer and novel therapeutic targets including PARP1. *Cancer Discov* 2012;2:798–811.
- Daniel VC, Marchionni L, Hierman JS, Rhodes JT, Devereux WL, Rudin CM, et al. A primary xenograft model of small-cell lung cancer reveals irreversible changes in gene expression imposed by culture in vitro. *Cancer Res* 2009;69:3364–73.
- Allison Stewart C, Tong P, Cardnell RJ, Sen T, Li L, Gay CM, et al. Dynamic variations in epithelial-to-mesenchymal transition (EMT), ATM, and SLFN11 govern response to PARP inhibitors and cisplatin in small cell lung cancer. *Oncotarget* 2017;8:28575–87.
- Williamson SC, Metcalf RL, Trapani F, Mohan S, Antonello J, Abbott B, et al. Vasculogenic mimicry in small cell lung cancer. *Nat Commun* 2016;7:13322.
- Haber DA, Velculescu VE. Blood-based analyses of cancer: circulating tumor cells and circulating tumor DNA. *Cancer Discov* 2014;4:650–61.
- Yu M, Bardia A, Wittner BS, Stott SL, Smas ME, Ting DT, et al. Circulating breast tumor cells exhibit dynamic changes in epithelial and mesenchymal composition. *Science* 2013;339:580–4.
- Yu M, Stott S, Toner M, Maheswaran S, Haber DA. Circulating tumor cells: approaches to isolation and characterization. *J Cell Biol* 2011;192:373–82.
- Carter L, Rothwell DG, Mesquita B, Smowton C, Leong HS, Fernandez-Gutierrez F, et al. Molecular analysis of circulating tumor cells identifies distinct copy-number profiles in patients with chemosensitive and chemorefractory small-cell lung cancer. *Nat Med* 2017;23:114–9.
- Bevilacqua S, Gallo M, Franco R, Rossi A, De Luca A, Rocco G, et al. A “live” biopsy in a small-cell lung cancer patient by detection of circulating tumor cells. *Lung Cancer* 2009;65:123–5.
- Hou J-M, Greystoke A, Lancashire L, Cummings J, Ward T, Board R, et al. Evaluation of circulating tumor cells and serological cell death biomarkers in small cell lung cancer patients undergoing chemotherapy. *Am J Pathol* 2009;175:808–16.

18. Hou J-M, Krebs MG, Lancashire L, Sloane R, Backen A, Swain RK, et al. Clinical significance and molecular characteristics of circulating tumor cells and circulating tumor microemboli in patients with small-cell lung cancer. *J Clin Oncol* 2012;30:525–32.
19. Naito T, Tanaka F, Ono A, Yoneda K, Takahashi T, Murakami H, et al. Prognostic impact of circulating tumor cells in patients with small cell lung cancer. *J Thorac Oncol* 2012;7:512–9.
20. Hodgkinson CL, Morrow CJ, Li Y, Metcalf RL, Rothwell DG, Trapani F, et al. Tumorigenicity and genetic profiling of circulating tumor cells in small-cell lung cancer. *Nat Med* 2014;20:897–903.
21. Dong Y, Skelley AM, Merdek KD, Sprott KM, Jiang C, Pierceall WE, et al. Microfluidics and circulating tumor cells. *J Mol Diagn* 2013;15:149–57.
22. George J, Lim JS, Jang SJ, Cun Y, Ozretic L, Kong G, et al. Comprehensive genomic profiles of small cell lung cancer. *Nature* 2015;524:47–53.
23. Rudin CM, Durinck S, Stawiski EW, Poirier JT, Modrusan Z, Shames DS, et al. Comprehensive genomic analysis identifies SOX2 as a frequently amplified gene in small-cell lung cancer. *Nat Genet* 2012;44:1111–6.
24. Peifer M, Fernandez-Cuesta L, Sos ML, George J, Seidel D, Kasper LH, et al. Integrative genome analyses identify key somatic driver mutations of small-cell lung cancer. *Nat Genet* 2012;44:1104–10.
25. Ben-David U, Ha G, Tseng YY, Greenwald NF, Oh C, Shih J, et al. Patient-derived xenografts undergo mouse-specific tumor evolution. *Nat Genet* 2017;49:1567–75.
26. Anderson WC, Boyd AM, Aguilar J, Pickell B, Laysang A, Pysz MA, et al. Initiation and characterization of small cell lung cancer patient-derived xenografts from ultrasound-guided transbronchial needle aspirates. *PLoS One* 2015;10:e0125255.
27. Ozkumur E, Shah AM, Ciciliano JC, Emmink BL, Miyamoto DT, Brachtel E, et al. Inertial focusing for tumor antigen-dependent and -independent sorting of rare circulating tumor cells. *Sci Transl Med* 2013;5:179ra47.
28. Karabacak NM, Spuhler PS, Fachin F, Lim EJ, Pai V, Ozkumur E, et al. Microfluidic, marker-free isolation of circulating tumor cells from blood samples. *Nat Protoc* 2014;9:694–710.
29. Harbour JW, Lai SL, Whang-Peng J, Gazdar AF, Minna JD, Kaye FJ. Abnormalities in structure and expression of the human retinoblastoma gene in SCLC. *Science* 1988;241:353–7.
30. Takahashi T, Nau MM, Chiba I, Birrer MJ, Rosenberg RK, Vinocour M, et al. p53: a frequent target for genetic abnormalities in lung cancer. *Science* 1989;246:491–4.
31. Heidorn SJ, Milagre C, Whittaker S, Nourry A, Niculescu-Duvas I, Dhomen N, et al. Kinase-dead BRAF and oncogenic RAS cooperate to drive tumor progression through CRAF. *Cell* 2010;140:209–21.
32. Cremolini C, Di Bartolomeo M, Amatu A, Antoniotti C, Moretto R, Berenato R, et al. BRAF codons 594 and 596 mutations identify a new molecular subtype of metastatic colorectal cancer at favorable prognosis. *Ann Oncol* 2015;26:2092–7.
33. Hainaut P, Pfeifer GP. Patterns of p53 G→T transversions in lung cancers reflect the primary mutagenic signature of DNA-damage by tobacco smoke. *Carcinogenesis* 2001;22:367–74.
34. Lim JS, Ibaseta A, Fischer MM, Cancilla B, O'Young G, Cristea S, et al. Intratumoural heterogeneity generated by Notch signalling promotes small-cell lung cancer. *Nature* 2017;545:360–4.
35. Saunders LR, Bankovich AJ, Anderson WC, Aujay MA, Bheddah S, Black K, et al. A DLL3-targeted antibody-drug conjugate eradicates high-grade pulmonary neuroendocrine tumor-initiating cells in vivo. *Sci Transl Med* 2015;7:302ra136.
36. Yen WC, Fischer MM, Axelrod F, Bond C, Cain J, Cancilla B, et al. Targeting Notch signaling with a Notch2/Notch3 antagonist (tarexumab) inhibits tumor growth and decreases tumor-initiating cell frequency. *Clin Cancer Res* 2015;21:2084–95.
37. Varghese AM, Zakowski MF, Yu HA, Won HH, Riely GJ, Krug LM, et al. Small-cell lung cancers in patients who never smoked cigarettes. *J Thorac Oncol* 2014;9:892–6.
38. Sequist LV, Waltman BA, Dias-Santagata D, Digumarthy S, Turke AB, Fidias P, et al. Genotypic and histological evolution of lung cancers acquiring resistance to EGFR inhibitors. *Sci Transl Med* 2011;3:75ra26.
39. Yu HA, Arcila ME, Rekhtman N, Sima CS, Zakowski MF, Pao W, et al. Analysis of tumor specimens at the time of acquired resistance to EGFR-TKI therapy in 155 patients with EGFR-mutant lung cancers. *Clin Cancer Res* 2013;19:2240–7.
40. Piotrowska Z, Niederst MJ, Karlovich CA, Wakelee HA, Neal JW, Mino-Kenudson M, et al. Heterogeneity underlies the emergence of EGFR T790M wild-type clones following treatment of T790M-positive cancers with a third-generation EGFR inhibitor. *Cancer Discov* 2015;5:713–22.
41. Lee JK, Lee J, Kim S, Kim S, Youk J, Park S, et al. Clonal history and genetic predictors of transformation into small-cell carcinomas from lung adenocarcinomas. *J Clin Oncol* 2017;35:3065–74.
42. Polley E, Kunkel M, Evans D, Silvers T, Delosh R, Laudeman J, et al. Small cell lung cancer screen of oncology drugs, investigational agents, and gene and microRNA expression. *J Natl Cancer Inst* 2016;108.
43. Townsend EC, Murakami MA, Christodoulou A, Christie AL, Koster J, DeSouza TA, et al. The public repository of xenografts enables discovery and randomized phase II-like trials in mice. *Cancer Cell* 2016;29:574–86.
44. Gao H, Korn JM, Ferretti S, Monahan JE, Wang Y, Singh M, et al. High-throughput screening using patient-derived tumor xenografts to predict clinical trial drug response. *Nat Med* 2015;21:1318–25.
45. Owonikoko TK, Behera M, Chen Z, Bhimani C, Curran WJ, Khuri FR, et al. A systematic analysis of efficacy of second-line chemotherapy in sensitive and refractory small-cell lung cancer. *J Thorac Oncol* 2012;7:866–72.
46. Lok BH, Gardner EE, Schneeberger VE, Ni A, Desmeules P, Rekhtman N, et al. PARP inhibitor activity correlates with SLFN11 expression and demonstrates synergy with temozolomide in small cell lung cancer. *Clin Cancer Res* 2017;23:523–35.
47. Subramanian A, Tamayo P, Mootha VK, Mukherjee S, Ebert BL, Gillette MA, et al. Gene set enrichment analysis: a knowledge-based approach for interpreting genome-wide expression profiles. *Proc Natl Acad Sci U S A* 2005;102:15545–50.
48. Liberzon A, Birger C, Thorvaldsdottir H, Ghandi M, Mesirov JP, Tamayo P. The Molecular Signatures Database (MSigDB) hallmark gene set collection. *Cell Syst* 2015;1:417–25.
49. Mollaoglu G, Guthrie MR, Bohm S, Bragelmann J, Can I, Ballieu PM, et al. MYC drives progression of small cell lung cancer to a variant neuroendocrine subtype with vulnerability to aurora kinase inhibition. *Cancer Cell* 2017;31:270–85.
50. Kuleshov MV, Jones MR, Rouillard AD, Fernandez NF, Duan Q, Wang Z, et al. Enrichr: a comprehensive gene set enrichment analysis web server 2016 update. *Nucleic Acids Res* 2016;44:W90–7.
51. Davis CA, Hitz BC, Sloan CA, Chan ET, Davidson JM, Gabdank I, et al. The Encyclopedia of DNA elements (ENCODE): data portal update. *Nucleic Acids Res* 2018;46:D794–801.
52. Jamal-Hanjani M, Wilson GA, McGranahan N, Birkbak NJ, Watkins TBK, Veeriah S, et al. Tracking the evolution of non-small-cell lung cancer. *N Engl J Med* 2017;376:2109–21.
53. Kim TM, Jung SH, An CH, Lee SH, Baek IP, Kim MS, et al. Sub-clonal genomic architectures of primary and metastatic colorectal cancer based on intratumoral genetic heterogeneity. *Clin Cancer Res* 2015;21:4461–72.
54. Harbst K, Lauss M, Cirenajwis H, Isaksson K, Rosengren F, Torngren T, et al. Multiregion whole-exome sequencing uncovers the genetic evolution and mutational heterogeneity of early-stage metastatic melanoma. *Cancer Res* 2016;76:4765–74.
55. Eirew P, Steif A, Khattra J, Ha G, Yap D, Farahani H, et al. Dynamics of genomic clones in breast cancer patient xenografts at single-cell resolution. *Nature* 2015;518:422–6.
56. Murai J, Feng Y, Yu GK, Ru Y, Tang SW, Shen Y, et al. Resistance to PARP inhibitors by SLFN11 inactivation can be overcome by ATR inhibition. *Oncotarget* 2016;7:76534–50.
57. Travis WD, Brambilla E, Nicholson AG, Yatabe Y, Austin JH, Beasley MB, et al. The 2015 World Health Organization classification of lung tumors: impact of genetic, clinical and radiologic advances since the 2004 classification. *J Thorac Oncol* 2015;10:1243–60.